

Interdecadal variability over the North Pacific in a multi-century climate simulation*

Andrew W. Robertson

Department of Atmospheric Sciences and Institute of Geophysics and Planetary Physics (IGPP), University of California, Los Angeles, 405 Hilgard Avenue, Los Angeles, USA

Received: 10 March 1995 / Accepted: 28 August 1995

Abstract. Interdecadal variability in the North Pacific region is investigated in a 500-y control integration of the Hamburg ECHAM+LSG coupled ocean-atmosphere general circulation model. The spectrum is predominantly red, but a significant peak with a period of about 18 y is detected in the spectrum of sea surface temperature (SST). This peak is shown to be associated with an irregular oscillation that involves both the model ocean and atmosphere. The SST, sea-level pressure, and geopotential height at 500 hPa all undergo a primarily standing oscillation with an extensive monopole structure centered near the date line. The surface anticyclone is situated to the northeast of the warm SST anomaly, and there is a small westward tilt with height; temporal changes are approximately in phase. The anomalous surface heat flux accompanying the warm phase of SST is primarily out of the ocean, but is compensated by anomalous warm advection by surface currents, allowing the SST anomaly to persist. Oceanic thermocline anomalies propagate northward in the western Pacific, and lag the atmosphere indicating a disequilibrium with the atmosphere; sub-surface thermal advection appears to play an important role. A comparison is made between the model's 18-y oscillation and oscillatory components identified in an analysis of the GISST observational SST dataset, which have periods of approximately 6 and roughly 30 y.

1 Introduction

Sea-surface temperatures (SSTs) over the North Pacific have been observed to fluctuate considerably on decadal time scales over the past half-century (Douglas et al. 1982; Trenberth 1990; Tanimoto et al. 1993). These variations have generated much recent interest because sizable correlations exist between North Pacific SSTs and diverse climatic indicators over North

America through down-stream teleconnections (e.g., Dickson and Namias 1976; Douglas et al. 1982; Trenberth and Hurrell 1994). The origins of interdecadal variability are still poorly understood. On intraseasonal time scales, the atmosphere over the North Pacific is believed essentially to drive the ocean, with changes in SSTs occurring one or two months later (e.g., Frankignoul 1985). On longer time scales, however, the coherent and simultaneous nature of atmospheric and oceanic variations is highly suggestive of ocean-atmosphere interaction, as documented early on by Namias (1959). Bjerknes (1964) and White and Barnett (1972) introduced the idea that fluctuations in poleward heat transport by the sub-tropical gyre together with atmospheric feedbacks, could produce oscillations on interdecadal time scales. Other authors, on the other hand, have suggested that the tropics are the primary driver of variability over the North Pacific (Graham 1994; Trenberth and Hurrell 1994).

The availability of data, together with the time scales involved, place severe limitations on what can be learnt from observations alone. Recent extended integrations with global coupled ocean-atmosphere general circulation models (GCMs) promise to help fill this gap. Using an albeit short 70-y integration of the Hamburg ECHO coupled GCM, Latif and Barnett (1994) conclude that mid-latitude air-sea interaction of the sort first envisaged by Bjerknes (1964) does occur in model's North Pacific with a period of roughly 20 y.

The aim of this study is to investigate, in detail, interdecadal variability in the North Pacific sector in a 500-y integration of the Hamburg ECHAM+LSG coupled ocean-atmosphere GCM. This integration is an extension of the 300-y integration examined by von Storch (1994), who identified a basin-wide oscillation in the Pacific Ocean with a time scale of 10–20 y. To make the analysis as objective as possible, we follow a two-part strategy, consisting of signal detection followed by optimal filtering. Firstly, the spectrum of SST variability is examined for statistically significant peaks with a Monte Carlo technique (Allen and Smith 1994, 1996; Robertson et al. 1995; Allen and Robertson 1995

* IGPP Contribution No. 4322

submitted) using 4-y means of SST. A statistically significant spectral peak does emerge, corresponding to a period of about 18 y. Having identified a peak, we then reconstruct the multivariate structure of the oscillation by optimally filtering annual-mean timeseries in the 5 to 25 y band. Atmospheric and oceanic variables are analyzed simultaneously to obtain a multivariate composite picture of the oscillation, from which the contribution of ocean-atmosphere interaction to the dynamics is investigated. Both stages of the analysis are based on multichannel singular spectrum analysis (M-SSA) (e.g., Plaut and Vautard 1994), an optimal filtering technique that can identify oscillatory behavior within a chosen spectral window. M-SSA is an empirical orthogonal function (EOF) analysis of lagged data, and the version employed here corresponds to a multichannel extension of the “method of delays” of Broomhead and King (1986).

The paper is organized as follows: in Sect. 2, we briefly review the coupled GCM and its climatology. Section 3 presents the signal detection part of the analyses. The multivariate structure of the oscillation is reconstructed in Sect. 4 in terms of a composite cycle. In Sect. 5, the model’s oscillation is compared to observed SST data, using M-SSA applied to the UK Meteorological Office’s GISST1 SST dataset (Parker et al. 1994), which spans the historical period 1871–1992. We conclude with a discussion and summary in Sect. 6. Details of the analysis methods are given in the appendices.

2 The coupled GCM

Details of the model and its climatology can be found in Cubasch et al. (1992) and von Storch (1994), who discuss the first 100 and 300 y of the present integration respectively. The atmospheric component (ECHAM1) is a low-resolution version of the numerical weather prediction model developed at the European Centre for Medium Range Weather Forecasts (ECMWF), that has been adapted for climate studies in Hamburg. In the horizontal, all variables are truncated triangularly at total wave number 21 (T21), and there are 19 levels in the vertical. The oceanic component (LSG) is based on a numerical formulation of the primitive equations appropriate for large-scale geostrophic motion, in which the nonlinear advection of momentum is neglected (Maier-Reimer et al. 1993). The ocean model, which is spun up over 7000 y, is global in extent and includes a simple sea-ice model; it has a similar (grid) resolution to the atmospheric model with 11 variably spaced vertical levels (the top layer is 50 m deep). The vertical mixing parameterization is a convective adjustment that is applied whenever the stratification becomes unstable. Coupling is synchronous, and a flux correction is applied to eliminate climate drift (Sausen et al. 1988).

Our analyses are based on annual averages over years 9–508. Figure 1 shows global maps of the standard deviation of unfiltered annual means for (a) SST,

(b) the upper-ocean heat content, and (c) the 500 hPa geopotential height. The North Pacific is a region of substantial variance in all three quantities, with standard deviations of the order of 0.5 K in SST, 0.3 K in heat content, and 15 m in the height of the 500 hPa geopotential surface over the Aleutian low. In the tropics, SST and heat-content variances are small; the model is unable to simulate the El Niño/Southern Oscillation (ENSO), principally because the low-resolution ocean model cannot resolve the associated equatorial wave dynamics.

To examine the North Pacific sector in detail, we select grid points within the range 20°N–60°N and 130°E–120°W. For atmospheric quantities these are on the AGCM’s 5.6° × 5.6° Gaussian grid, while SST and ocean quantities are on two overlapping 5.6° × 5.6° grids giving an effective net grid size of about 4°.

3 Signal detection

Empirical orthogonal function (EOF)-based analyses such as M-SSA are often hampered by the difficulty of distinguishing between “signal” and “noise” patterns. Climatic time series are inherently “red” in both space and time, so that the leading EOFs are generally characterized by large spatial scales and large decorrelation times; these can often appear deceptively similar to large-scale low-frequency oscillatory signals. The natural null-hypothesis to test oscillatory M-SSA patterns against, is that the time series has been generated by a first-order autoregressive [AR(1)] process, i.e., red noise. This test is a multichannel extension of the Monte Carlo test developed by Allen and Smith (1994, 1996) for single-channel SSA, and is described in Robertson et al. (1995) and Allen and Robertson (1995 submitted); an outline is given in Appendix A.

The spectrum of power against frequency shown in Fig. 2 is the result of the test applied to 4-y means of SST over the North Pacific (i.e., the temperature in the uppermost layer of the OGCM, which extends to 50 m). Diamonds denote the power contained in the GCM’s SST field, while the error bars indicate the 90% confidence interval of the AR(1) noise null-hypothesis, generated using 1000 surrogate noise time series (see Appendix A). The only frequency in the GCM time series with more power than expected at the 95% confidence level is at 0.057 cy/y, or a period of about 17.5 y. Note how the power in the large ensemble of noise surrogate-data segments, the error bars, decreases almost monotonically with increasing frequency, characteristic of a red process. The steepening of the noise spectrum at low frequencies stems from the dependence of decorrelation time on spatial scale. Further explanation is given in Appendix A.

The GCM time series contains less power than expected of the null-hypothesis at two sample frequencies near 0.050 cy/year. Since the AR(1) surrogate data have been constructed to “fit” the GCM sample time-series (Appendix A), it is natural that if there are excursions of the GCM data above the error bars at some

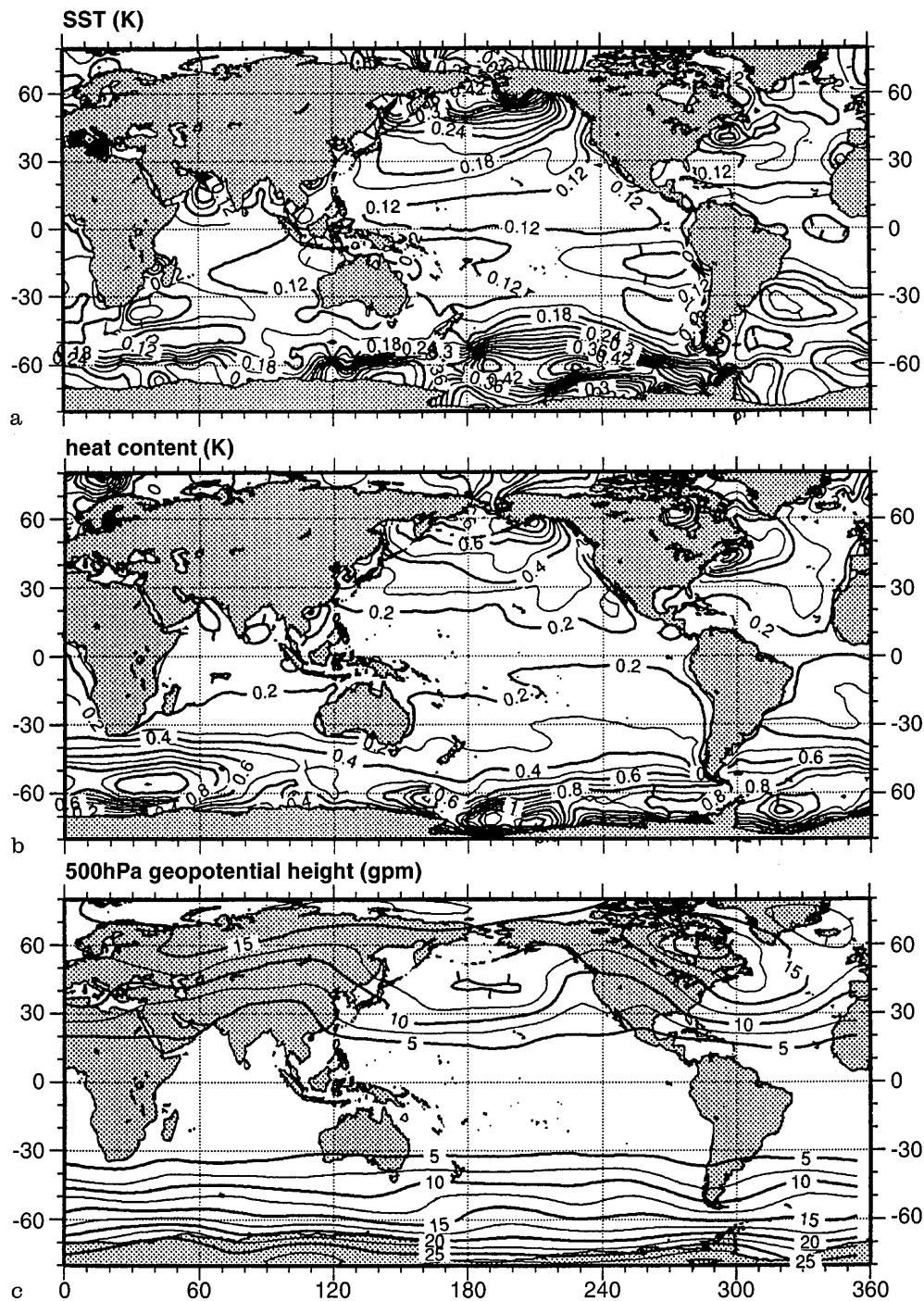


Fig. 1. **a** Standard deviation of annual means of SST (K), **b** upper-ocean heat content (the temperature averaged between 50–575 m depth) (K), and **c** geopotential height of 500 mb surface (gpm)

frequencies, there will be excursions below at others. Following standard practice in spectral analysis (e.g., Thomson 1990), confidence levels apply to the local tests of individual basis vectors. However, although there are effectively 115 such tests in Fig. 2, these tests are not independent so that the total number of excursions outside the 90% confidence limits expected just by chance can be much less than 11. These issues are discussed in detail in Allen and Smith (1996).

4 Signal reconstruction

Having detected a frequency in the coupled GCM's SST time series with significantly more power than expected of appropriate red noise, the second step is to reconstruct the multivariate structure associated with it using M-SSA. To explore the possibility that the underlying dynamics involve ocean-atmosphere interaction, the following variables are analyzed simultaneously over the North Pacific: geopotential height at 500 hPa, sea-level pressure (SLP), the net heat flux

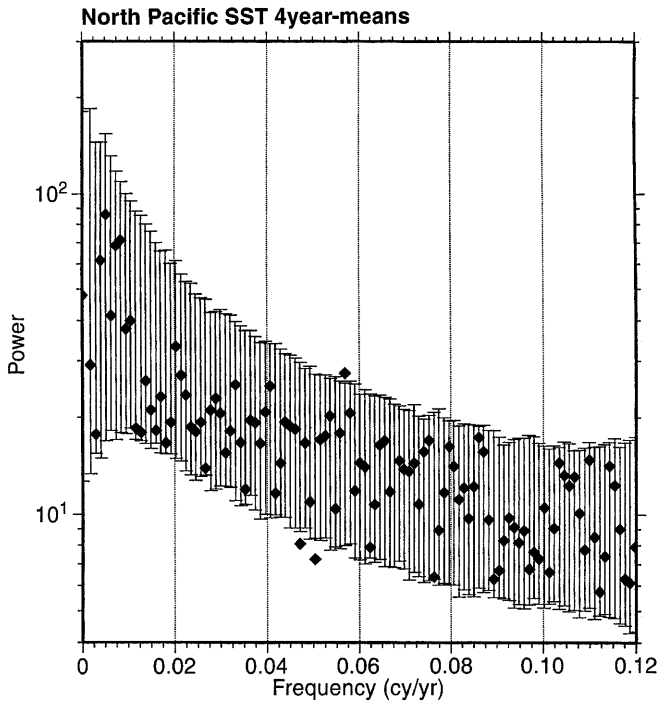


Fig. 2. Monte-Carlo significance test of coupled GCM's North Pacific SST (4-y means). Shown are projections of North Pacific SST onto the AR(1) null-hypothesis basis, versus the dominant frequency of the basis vectors. The latter were computed via a reduced Fourier transform. The error bars show the 90% confidence interval of an AR(1) noise null hypothesis, generated using 1000 segments of noise, see Appendix A for details

into the ocean, the SST, the oceanic heat content (defined as the vertical average of temperature between 50 and 575 m, i.e., model layers 2–5), and the currents at 150 m depth. The frequency of the oscillation under scrutiny has been identified, so the signal-to-noise (S/N) ratio can be enhanced by temporal filtering prior to M-SSA.

At each grid point, annual means of each of these 7 variables were first bandpass filtered, retaining periods between 5 and 25 years as described in Appendix B, and then normalized by their standard deviations. Next, each variable (grid point field) was compressed separately via a spatial EOF expansion, and the resulting 10 leading spatial principal components (S-PCs) pooled before a second combined (unnormalized) EOF analysis; the leading 10 PCs of the latter (69.8% of the variance) form the channels for M-SSA. The results of these EOF analyses are tabulated in Table 1. This two-step compression firstly selects patterns of spatial correlation in each variable, and then selects the leading components of covariance between them

Table 1. Percentage variance in leading ten spatial PCs of each North Pacific filtered field

Variable	SST	Sea-level pressure	500 hPa height	Surface heat flux	Heat content	150 m u-velocity	150 m v-velocity
%	69.9	87.5	88.2	51.3	72.9	73.5	63.6

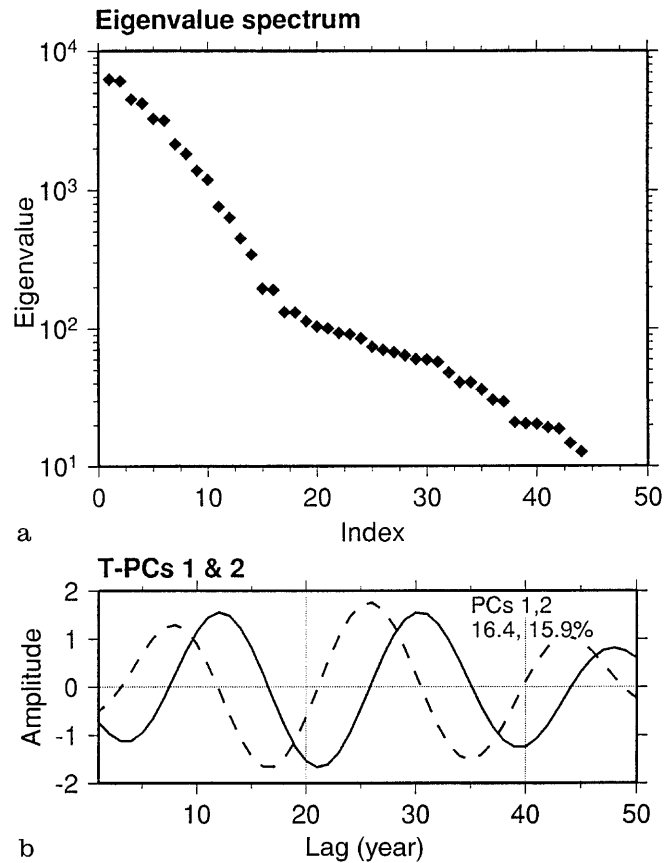


Fig. 3a, b. Combined 7-variable M-SSA of North Pacific region, **a** eigenvalue spectrum, **b** leading pair of temporal principal components (T-PCs). The variance associated with each T-PC is given in the *top-right corner*

(Xu 1993). It makes the multivariate problem tractable by compressing a ~ 1700 spatial grid-point time series into just 10 channels in an optimal way.

Figure 3 shows the eigenspectrum of a combined 7-variable M-SSA, together with the leading pair of temporal PCs. Details of the M-SSA procedure are given in Appendix A. The eigenvalues of the leading two eigenmodes form a pair that is well separated from those of modes 3 and 4 (Fig. 3a), and accounts for 32.3% of the filtered variance. Pairing of eigenvalues in M-SSA is often associated with oscillatory behavior (Vautard and Ghil 1989). This is confirmed to be the case for modes 1 and 2 because the associated PCs (Fig. 3b) are near-sinusoidal and in phase-quadrature with one another. The PCs associated with modes 3–6, on the other hand, are far from sinusoidal (not shown).

To examine the temporal evolution of the leading modal pair and its structure, we reconstruct in physical

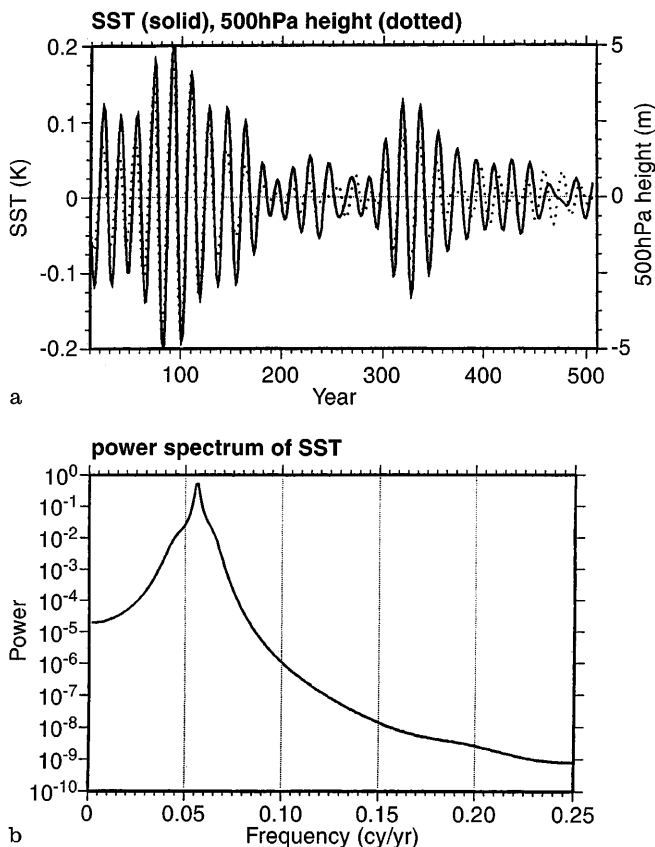


Fig. 4. **a** Indices of spatial averages of RCs 1–2 for SST over ($30\text{--}40^\circ\text{N}$, $160\text{--}180^\circ\text{E}$) (solid line), and 500 hPa geopotential height over ($30\text{--}60^\circ\text{N}$, $160\text{--}180^\circ\text{E}$) (dotted). **b** Power spectrum of SST index, computed using MEM with 20 poles

space the component of the original time series associated with it. Figure 4a shows the *reconstructed components* (RCs 1 and 2; Vautard et al. 1992) of SST averaged over the region ($30\text{--}40^\circ\text{N}$, $160\text{--}180^\circ\text{E}$) (solid line), and the geopotential height at 500 hPa averaged over the region ($30\text{--}60^\circ\text{N}$, $160\text{--}180^\circ\text{E}$) (dotted line); these are the regions of maximum respective modal variance (not shown). RCs 1–2 are most pronounced around year 100 when both SST and geopotential height vary in unison, with a weaker spell of activity around year 350. The maximum amplitude of SST variation is about 0.2 K, which is accompanied by geopotential fluctuations of about 5 m; i.e., a ratio of about 25 m/K. This ratio is similar to that found over the North Atlantic by Palmer and Sun (1985) in an AGCM forced with observed SST anomalies, but much smaller than that in the coupled model of Latif and Barnett (1994). Figure 4b shows the power spectrum of the SST index in Fig. 4a, computed using the maximum entropy method (MEM) with 20 poles (e.g., Dettinger et al. 1995). Although the associated oscillatory behavior is intermittent (Fig. 4a), the power spectrum still enables us to estimate its frequency. The spectrum is sharply peaked at about 0.056 cy/y (a period of about 18 y), in full agreement with the value of 0.057 cy/y obtained

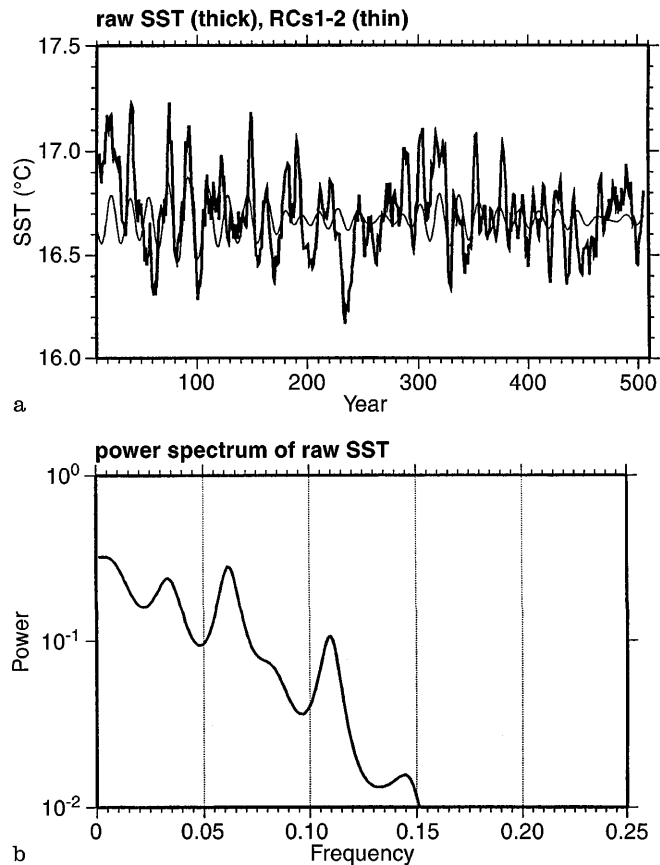


Fig. 5. **a** Time series of “raw” SST averaged over the region ($30^\circ\text{N}\text{--}40^\circ\text{N}$, $160^\circ\text{--}180^\circ\text{E}$) (thick line), together with RCs 1–2 from Fig. 4a. A 5-y running smoother has been applied to the raw data. **b** Power spectrum of raw SST index, computed using MEM with 40 poles

with the AR(1) basis in Sect. 3, to within the spectral resolution.

Is such an evolution of SST visible in the raw data? Figure 5a shows the *total* model SST averaged over the same region as in Fig. 4, smoothed with a 5-y running mean (thick line); RCs 1–2 from Fig. 4a are superposed (thin line). The raw time series is very irregular with large variations of over 0.5°C . RCs 1 and 2 generally only account for a small fraction of these variations, though the fraction becomes quite large around year 100. The oscillation that they represent can be interpreted as an underlying weakly-unstable periodic orbit within the system’s attractor (Vautard et al. 1992), whose amplitude is relatively weak. The power spectrum of the raw time series is plotted in Fig. 5b. It has peaks at about 16 and 9 y, but the S/N ratio is much smaller than that of RCs 1–2 in Fig. 4b (note the different scales of the ordinates). The leading modes of a single-channel SSA (e.g., Dettinger et al. 1995) of the raw SST time series in Fig. 5a have periods of about 33 and 17 y and explain about 15 and 13% of the variability respectively. Even here the amplitudes of the RCs (not shown) are only ~ 0.1 K, which is further testimony to the irregular character of the oscillation.

To examine the structure of the 18-y oscillation, a

composite cycle of RCs 1–2 is constructed by selecting all SST-peaks in Fig. 4a that exceed +0.1 K (ten in all), and compositing the 9 y (i.e., approximately half the period) either side of each peak. Figure 6 shows the result of this phase-compositing on the indices in Fig.

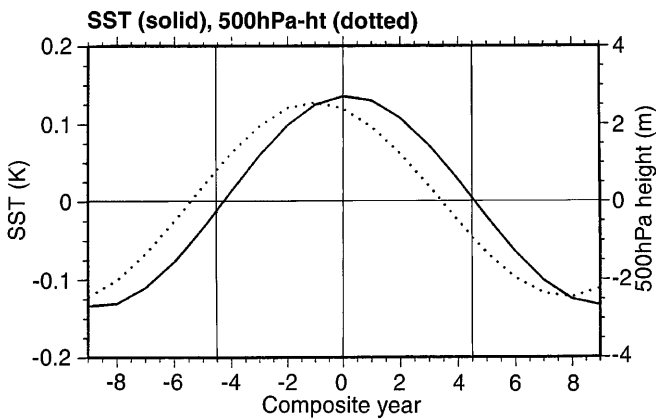


Fig. 6. Composite cycle of RCs 1–2 for SST over (30–40°N, 160–180°E) (solid line), and 500 hPa geopotential height over (30–60°N, 160–180°E) (dotted)

4a. The cycle of SST closely approximates a cosine curve, lending credence to the simple compositing procedure. The geopotential height at 500 hPa is also near-cosinusoidal, and leads SST by about 1 y. The sea-level pressure (SLP) averaged over the same box as 500 hPa height varies in phase with the latter (not shown).

Composite maps of the oscillation are shown in Figs. 7, 8 and 10, where grid boxes which pass a t-test at the 99% level are stippled. Anomalies of SST, SLP and geopotential height at 500 hPa are each predominantly stationary. Figure 7 shows the peak-positive (y 0) and approximate quadrature phase (y +4) of the composite cycle for these three variables. In the peak phase, above normal SSTs cover most of the North Pacific west of 160°W, with a small area of large below-normal values over the Gulf of Alaska. Geopotential height and SLP both have extensive monopoles of the same sign as SST; the 500 hPa ridge is centered about 10° due north of the SST maximum, with the surface anticyclone centered to the northeast of the SST anomaly. There is some westward tilt with height in the pressure field. The quadrature phase (y +4) is characterized by relatively weak anomalies in all three variables.

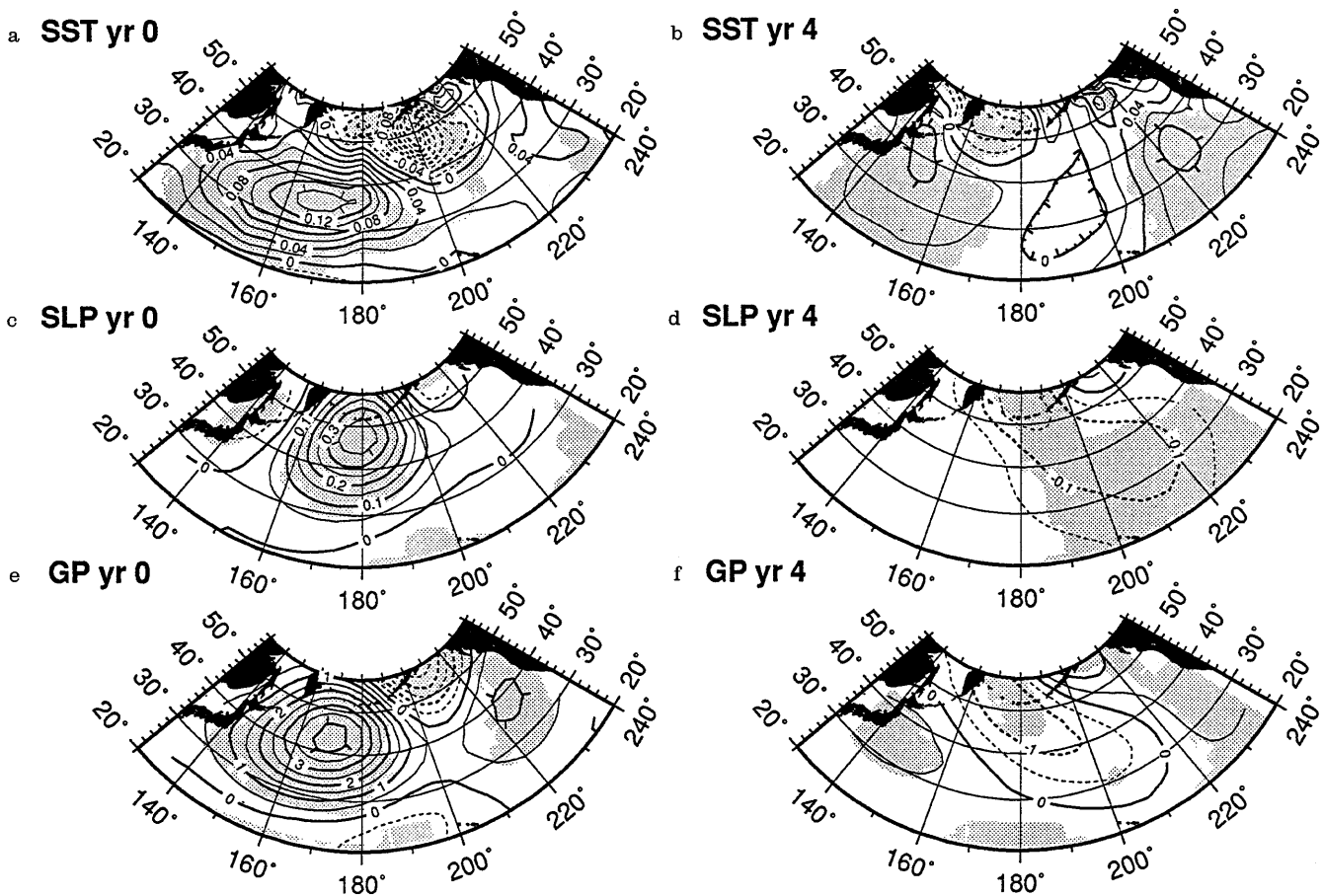


Fig. 7a–f. Composite maps of RCs 1–2 at y 0 and +4 of the cycle in Fig. 6. **a** and **b** SST (contour interval 0.02 K); **c** and **d** sea-level pressure (contour interval 0.05 mb); **e** and **f** geopotential height at 500 hPa (contour interval 0.5 gpm). Negative anomalies

dashed. Stippling indicates those grid boxes where a t-test on the mean of the 10 events in the composite exceeds the 99% significance level

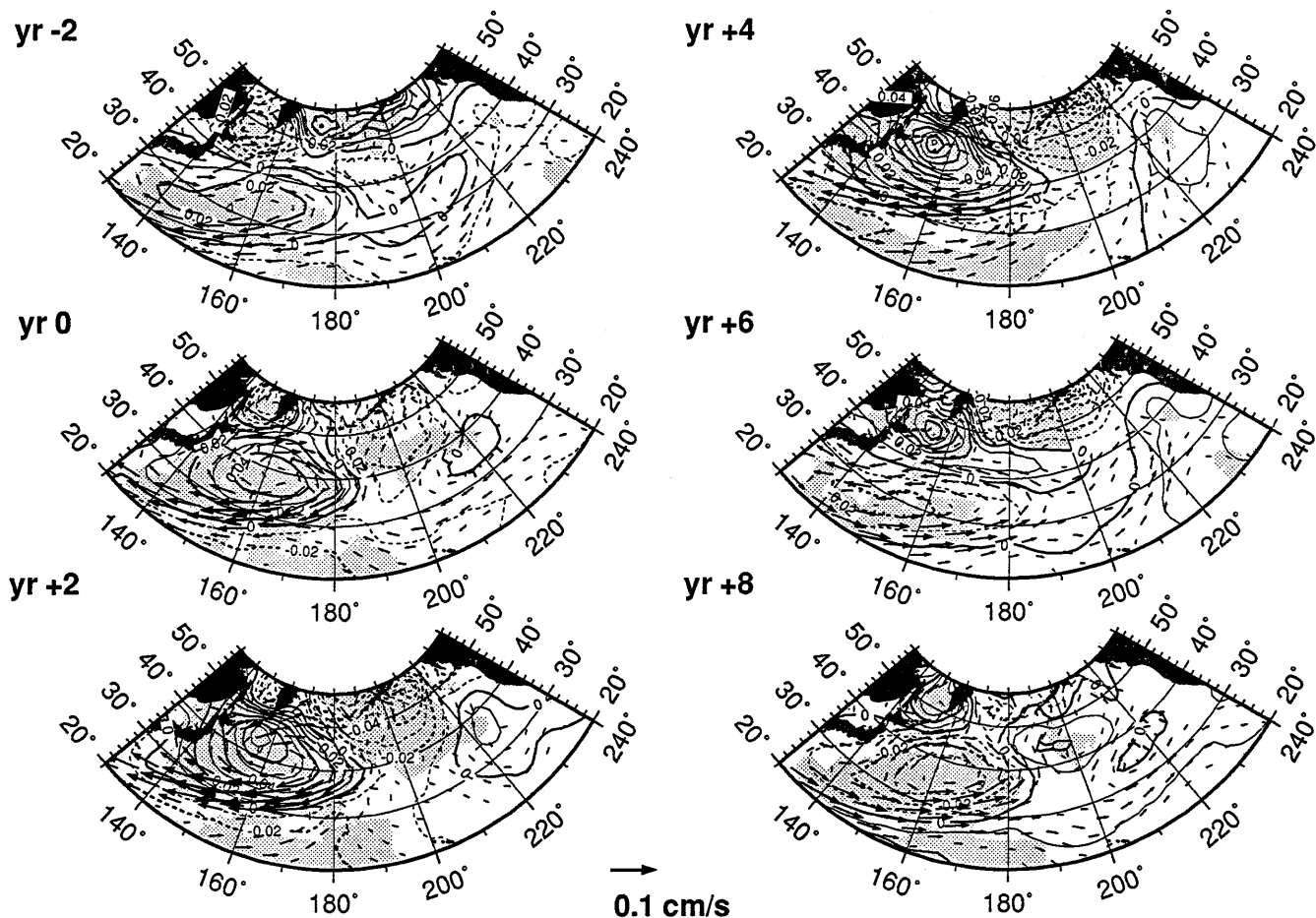


Fig. 8. Composite maps of RCs 1–2: oceanic heat content (contours every 0.01 K) and current at 150 m at $y - 2$, 0, +2, +4, +6, and +8 of cycle in Fig. 6. As Fig. 7

Similar results are obtained if the M-SSA is applied to each variable separately, and there is little amplitude in SST south of 20°N when the domain is extended to the equator. As a check on the spatial pattern of SST in Fig. 7a, a correlation map of SST was constructed using the SST time series in Fig. 4a as an index. The result (not shown) is similar to Fig. 7a, and the similarity increases if SST is detrended; correlations are weak south of 20°N . The extent to which this structure occurs in observed data is investigated in Sect. 5 later.

Figure 8 shows the evolution of oceanic heat content and 150 m-depth ocean currents in terms of composite anomaly snapshots every 2 y, from $y - 2$ (just before the peak in geopotential height; Fig. 6) to $y + 8$. The 150 m current anomaly vectors show the expected qualitative geostrophic balance with the anomalies of heat content (50–575 m temperature), lending credence to our analysis methods, and indicating that the latter vertical average well represents the anomalies in the thermocline. Heat-content anomalies in the western Pacific propagate northward and intensify, suggestive of the mean gyral circulation. This contrasts with the largely standing character of SST, SLP, and 500 hPa height anomalies. The attendant current anomal-

ies do modulate the northern flank of the subtropical gyre, whose mean position lies between $30\text{--}40^{\circ}\text{N}$ as shown in Fig. 9, but the anomaly amplitudes are clearly only a fraction of the mean. Oceanic anomalies are largest toward the western boundary and have spatial scales of the order of the atmospheric Rossby radius, indicating the influence of the atmosphere. The largest current anomalies occur at about $y + 2$ and thus lag those in geopotential height and SLP by about 4 y.

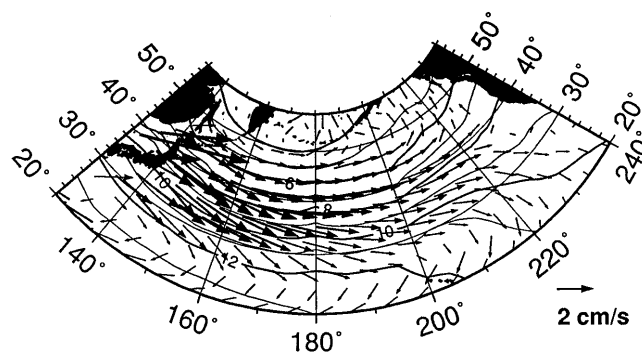


Fig. 9. Climatological mean ocean heat content (contours every 1°C) and currents at 150 m depth

This indicates that the ocean is not in Sverdrup balance with the wind stress, and that time scale of oceanic adjustment to wind-stress and surface heat flux changes is important. Furthermore, the appearance of the negative heat content anomaly over the western Pacific around $y + 6$, lags the occurrence of the large negative current anomalies there ($\sim y + 2$) by about 4 y, suggesting that sub-surface thermal advection may be important.

To explore the roles of oceanic thermal advection and the surface heat flux, the associated composites are shown in Fig. 10 for $y 0$ and $+4$. Advection anomalies associated with the oscillatory RC pair are approximated as the linear sum $\bar{\mathbf{v}}' \cdot \nabla \bar{T} + \bar{\mathbf{v}} \cdot \nabla T'$, where the overbar denotes the 500-y time average, and the prime RCs 1–2. This sum is computed at 25 m and 150 m depth for each member of the composite events in Fig. 6 before compositing. Simple centered differencing is used. To obtain the surface-current anomalies, the 7-variable M-SSA was repeated but with the currents at 25 m substituted for those at 150 m; the 150 m temperature anomalies were obtained similarly.

The anomalous surface heat flux associated with the warm SST anomaly at $y 0$ (Fig. 10a) is largely out of the ocean, with an area heat flux into the ocean to the

northwest. There is a zonal phase shift between the sea-level pressure (SLP) and heat-flux anomalies, which suggests that atmospheric anomalous cold advection to the east of the surface anticyclone in Fig. 9c is balancing the anomalous surface heat flux into the atmosphere, with the signs reversed to the west of the anticyclone. In the absence of other effects, this surface-flux pattern would tend to make the SST anomaly propagate westward; it is the signature of a baroclinic Rossby wave.

The large heat flux anomalies over the Aleutians are also consistent with Fig. 7c and appear to be associated with the negative pole of the SST pattern. Figure 10b shows that the surface heat flux has an appreciable non-stationary component, and there is an indication that off the east coast of Asia, the heat-content anomalies in Fig. 8 are being forced thermally from the surface, perhaps associated with strong convective mixing there in winter.

Figure 10c shows that the surface heat flux out of the ocean on the eastern flank of the warm SST anomaly is compensated by large anomalous warm advection in the surface layer of the ocean. Advection of the mean temperature field by anomalous currents is the larger component (not shown), and is in-phase both

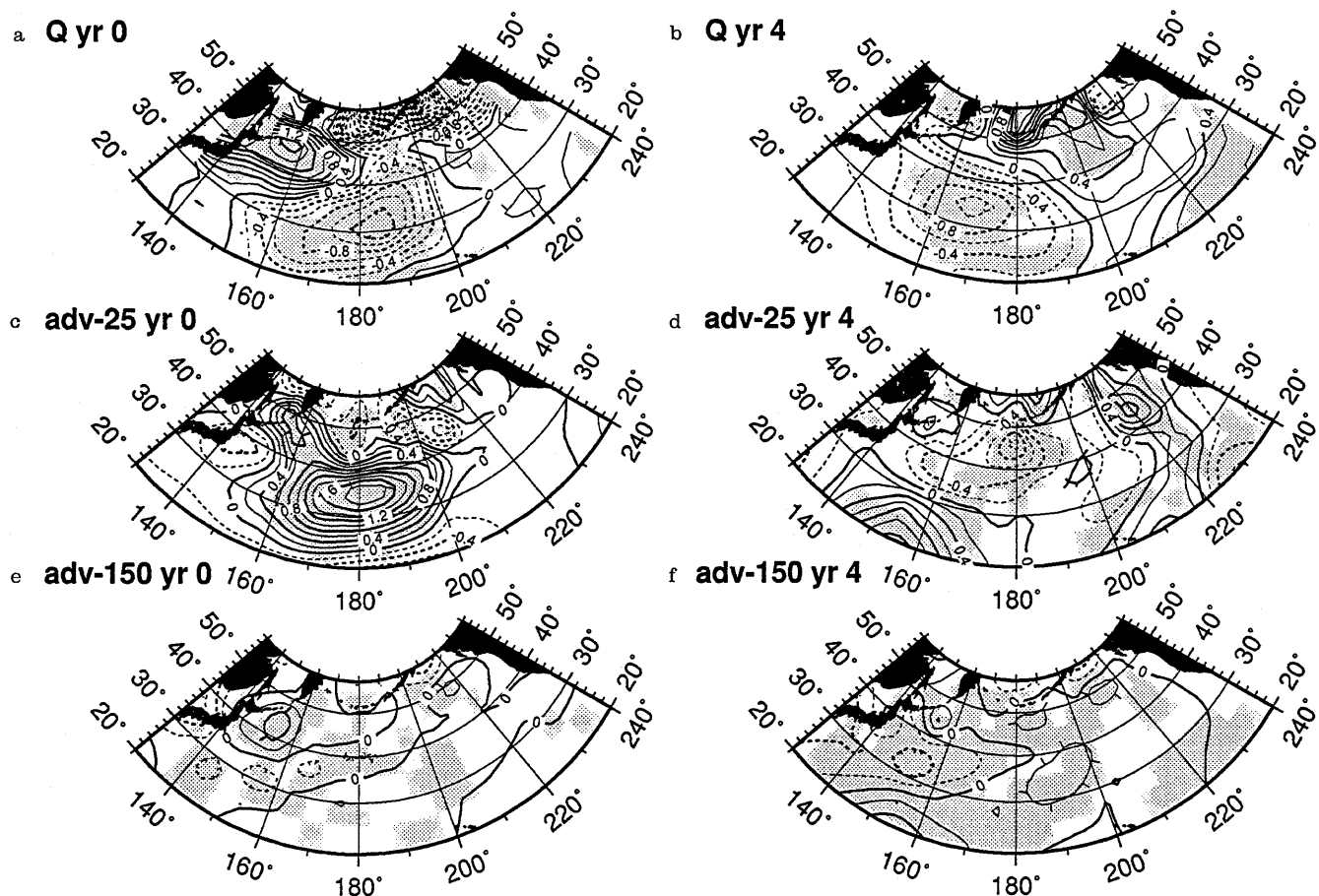


Fig. 10a–f. As Fig. 7, but for **a** and **b** net heat flux into the ocean; **c** and **d** surface-layer advective temperature tendency; **e** and **f** advective tendency at 150 m. Contour interval is 0.2 K/decade, with

the surface heat flux assumed to be distributed over a 50 m depth of water

spatially and temporally with the SST anomaly, thus tending to amplify it. This advective warming to the south of the anticyclone in Fig. 7c is consistent with the implied Ekman current anomalies. However, advection of anomalous SST by the mean surface currents is nonetheless significant, and the net effect gives an eastward propagating tendency to the SST anomaly. Palmer and Sun (1985) postulated that a balance between the surface heat flux and advection by anomalous Ekman currents could lead to persistence of SST anomalies, while Miller (1992) has discussed this further and noted the possibility of eastward propagation. In the coupled GCM, the pronounced persistence and stationarity of the SST anomaly appears to be due to the action of two opposing effects: the anomalous surface flux which tends to make the SST anomaly propagate westward, and the oceanic thermal advection which produces an eastward propagating tendency. Both effects are tied together by the SST-SLP anomaly spatial configuration.

Below the surface at 150 m depth, anomalous cold advection in the Kuroshio extension region is pronounced at y 4 (Fig. 10f), which is consistent with the anomalous currents in Fig. 8. Advection at y 4 is dominated by the effect of the anomalous currents on the mean thermal gradient, while at y 0 advection by the mean gyre reaches comparable magnitude. Sub-surface advection thus appears to lead the thermal anomalies

in this region by about a quarter period, suggesting that the latter are advectively forced by the sub-surface ocean.

Regional indices can help clarify these important temporal phase relationships. Figure 11 shows the sub-surface thermal evolution at 150 m depth for (a) the region of maximum SST anomaly (“maxSST” hereafter; 160–180°E, 30–40°N), and (b) the region south of the Kuroshio extension to the southwest (140–160°E, 25–35°N). Over maxSST (Fig. 11a), the 150 m temperature anomaly (solid line) peaks slightly after SST, while sub-surface advection (dotted line) tends largely to damp the sub-surface anomaly. To the southwest (Fig. 11b), the 150 m temperature anomaly (solid line) peaks at y –2, which is just prior to the mid-tropospheric anomaly. Thus, although the latter leads SST over maxSST by 1 y in Fig. 6, the heat-content anomaly to the southwest precedes it. Here advection (dotted line) *leads* the thermal anomaly by about one-quarter period, consistent with advective forcing as suggested in Fig. 10f. The residual of the heat balance (crosses) includes the effects of vertical advection and mixing, together with analysis error; it is of the same order as the advection.

Turning to the surface layer over maxSST (Fig. 12a, note different ordinate scales), the surface heat flux (dashed line) leads SST by about one-quarter period, implying atmospheric forcing, while horizontal advective

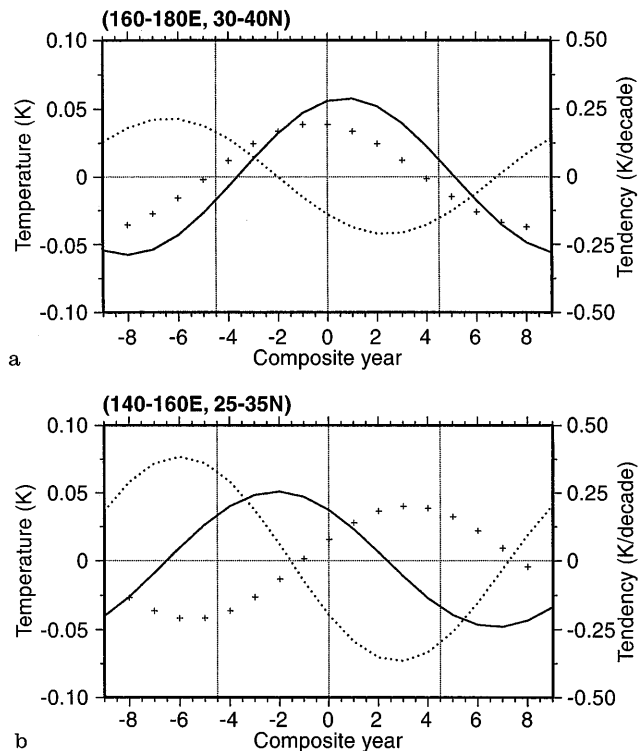


Fig. 11a, b. Composite cycle of 150 m temperature (solid line) and advective tendency (dotted line) averaged over the regions **a** (160–180°E, 30–40°N), and **b** (140–160°E, 25–35°N). Crosses denote the residual of the heat budget

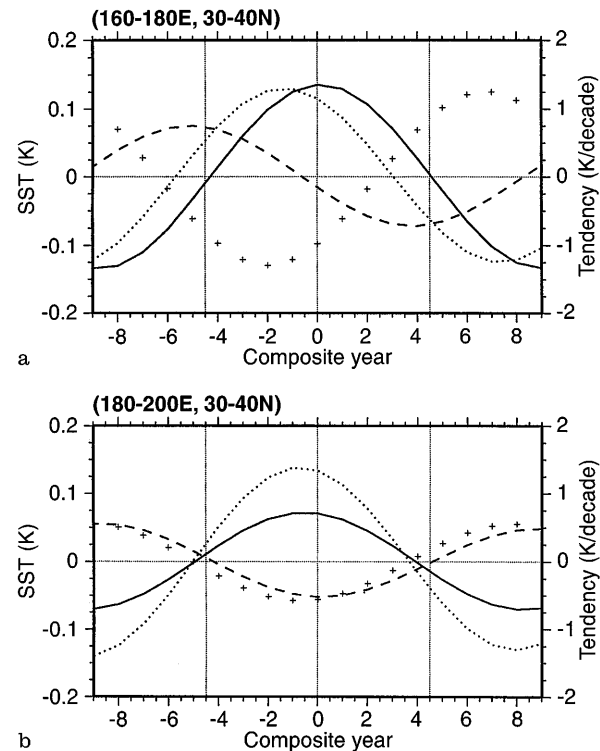


Fig. 12a, b. Composite cycle of surface layer temperature (SST, solid line), advective tendency (dotted line), and heat flux into the ocean (dashed line) averaged over the regions **a** (160–180°E, 30–40°N), and **b** (180–160°W, 30–40°N). Crosses denote the residual of the heat budget. The surface heat flux is assumed to be distributed over a 50 m depth of water

tion (dotted line) is of larger amplitude and nearly in phase, implying amplification of the SST anomaly. The residual of the heat balance (crosses) offsets advection, suggesting that vertical transport may act to deepen the anomaly. To the east of maxSST (Fig. 12b; 180°–160°W, 30–40°N) the near in-phase relationships indicate that surface-layer advection acts to amplify the SST anomaly, while the surface heat flux acts to damp it.

To summarize, there is evidence that the spatial configuration of the SST and SLP anomalies allow the SST anomaly to persist through a compensation between the surface heat flux anomaly, and opposing thermal advection in the surface layers of the ocean and atmosphere. Beneath the ocean surface layer, anomalous warm advection to the southwest precedes the warm SST anomaly, suggesting that the sub-surface ocean plays an important role.

5 Analysis of GISST observed SST data

The SST anomaly pattern in Fig. 4a associated with the model's 18-y oscillation resembles the observed SST anomaly of 1977–88 (Trenberth and Hurrell 1994) and is not unlike the leading spatial EOF of the COADS data lowpass filtered at 5 y (Tanimoto et al. 1993). The GCM's SST anomaly maximum is displaced about 10–20° west of the observed position, which is consistent with the model's climatological Aleutian low being centered too far west (Latif personal communication). The approximate in-phase relation, both spatially and temporally, between decadal anomalies of SST and geopotential height over the North Pacific was also found by Latif and Barnett (1994). It has also been found on interannual time scales in observed data by Wallace et al. (1990), where the atmospheric pattern corresponds to the Pacific/North American (PNA) pattern.

To explore further the relevance of the model's 18-y oscillation to the real world, we have applied M-SSA to the UK Meteorological Office's GISST SST observational dataset 1871–1992, version 1.2 (Parker et al. 1994). GISST is a gridded extension of the Meteorological Office Historical Sea Surface Temperature (MOHSST) dataset that includes COADS data. Interpolation in time and space uses a Laplacian-based scheme, with a relaxation to climatology included. Details can be found in Parker et al. (1994).

Using annual means of SST on a 5° × 5° latitude-longitude grid for the same North Pacific domain considered already, we repeat the signal detection and reconstruction procedures used for the GCM. As in the analysis of the GCM, only ice-free grid points are included. Figure 13 shows the Monte-Carlo significance test against red noise, using the leading 10 S-PCs of annual-mean SST (86% of the total variance), and $N_w = 115$ y. At the 95% confidence level, the only frequencies with anomalously more power than red noise in the GISST data over the North Pacific corresponds to a period of about 5.7 y, and the trend. The 5.7 y frequency also

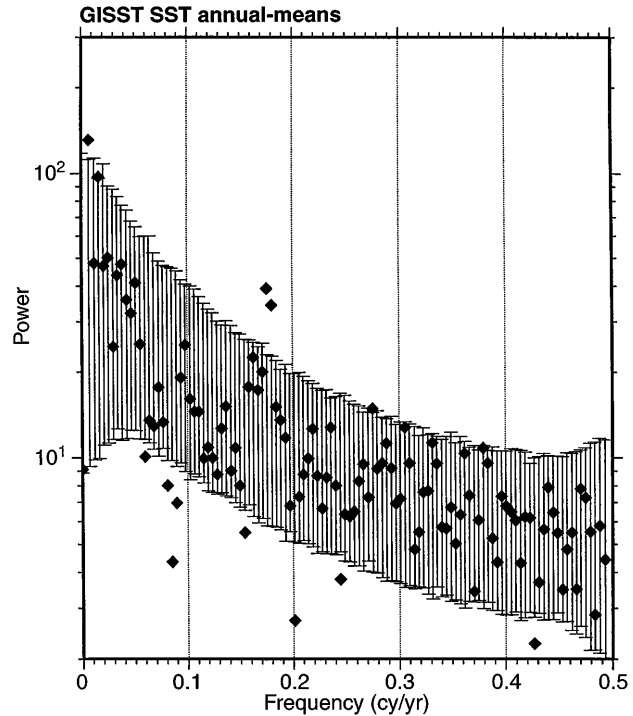


Fig. 13. Monte-Carlo significance test of North Pacific GISST annual mean SSTs. The error bars indicate the 90% confidence interval of the AR(1) noise null hypothesis. As Fig. 2

passes the test at the 97.5% level, which is higher than the 18-y mode in the GCM.

M-SSA was then applied to the leading 10 S-PCs to reconstruct the spatial structure of the oscillation. The trend was removed at the outset using the SSA detrending algorithm with a filter-length of 50 y, and M-SSA then applied to the S-PCs of the detrended time series with $N_w = 40$ y. The main features of the result are insensitive to retaining the trend, or using $N_w = 30$ –50 y. The resulting eigenvalue spectrum (not shown) exhibits a leading pair of eigenvalues (8.2% and 7.3% of the variance), followed by a second near-equal pair (5.9% and 5.9%). The RCs (reconstructed components) associated with these two pairs are plotted at (35–40°N, 150–155°W) in Fig. 14 together with the raw data; this is a location where both pairs have large variance (not shown). Figure 14a shows that both pairs are associated with oscillatory components of the time series; the graver oscillation, RCs 1–2, has a period of about 30 y (by applying MEM, not shown), while RCs 3–4 have a period of 5.8 y and correspond to the statistically significant peak in Fig. 13. The peak amplitudes of the RCs are about double those of the GCM. RCs 1–4 together account for 27.3% of the total SST variance in the 1 to 40-y band over the entire North Pacific domain. Figure 14b indicates, however, that the agreement with the raw data is rather poor over this particular grid box; it is closer further west (not shown).

Composite maps of the peak-positive and transition phases of each oscillatory RC pair are plotted in Fig. 15, keeping in mind that the 30-y component is not sta-

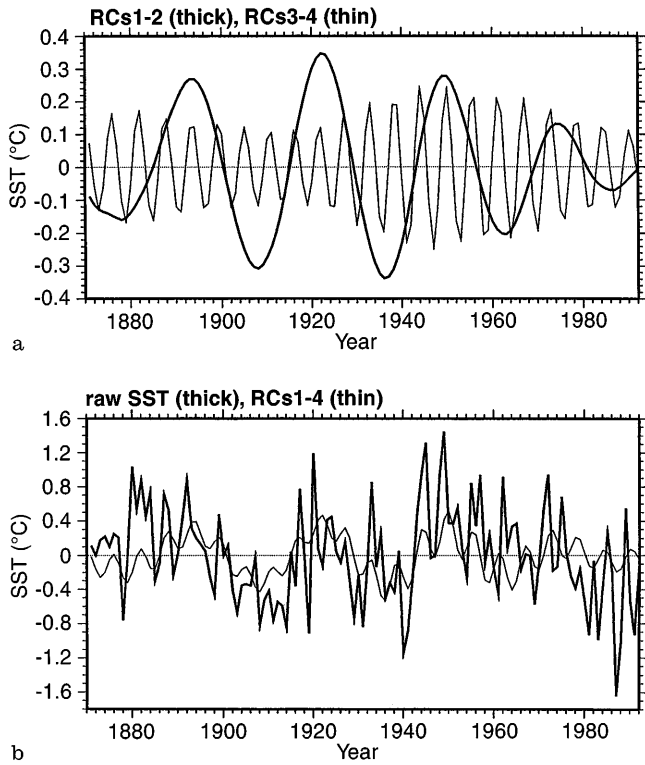


Fig. 14a, b. Indices of the leading two GISST RC pairs over the 5° -box ($35\text{--}40^\circ\text{N}$, $150\text{--}155^\circ\text{W}$). **a** RCs 1–2 (thick line), and RCs 3–4 (thin line); **b** raw GISST SST (thick line), and the sum RCs 1–4 (thin line)

tistically significant. For the peak phase we composite all annual maxima that exceed $+0.2^\circ\text{C}$ in Fig. 14a, while the transition phase is constructed by compositing the following approximate zero crossing. The patterns were checked against their opposite-phase counterparts and found to be similar. Both the 30-y and 6-y oscillatory components have quite similar spatial structures which are predominantly stationary, while the 6-y component exhibits some northeastward propagation. There is a broad similarity with the model's 18-y oscillation, although the 30-y component composite fails the 99% t-test over the west Pacific. The main difference from the GCM is the much larger zonal extent of the observed anomaly composites. The resemblance to the 6-y component is especially clear, with the sign change to the west and northwest.

The spatial structures of the GISST anomalies in Fig. 15 resemble the leading spatial EOF of COADS SST of Wallace et al. (1990), and Tanimoto et al. (1993). The 30-y component agrees with the 27-y period component in global-mean temperatures and its associated structure in North Pacific SST found by Allen and Smith (1994). The 6-y time scale has also been found by Sezginer and Ghil (1995) in an analysis of North Pacific sea-level station data and is likely to be associated with ENSO.

6 Discussion

An oscillation with a period of about 18 y is present in the ocean and atmosphere of the North Pacific in a 500 y integration of the Hamburg ECHAM+LSG cou-

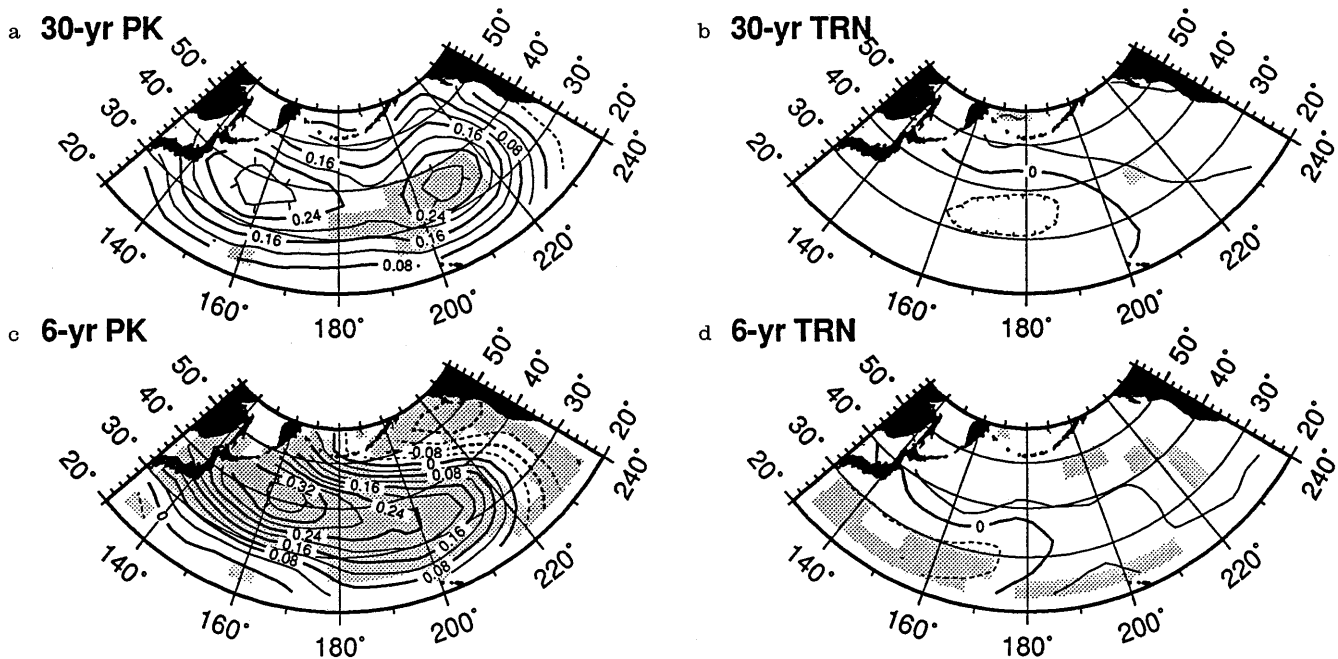


Fig. 15a–d. Composite maps of GISST RCs 1–2 (30-y component) and RCs 3–4 (6-y component), for the peak positive phase of the cycle and the following quadrature transition phase. **a** RCs 1–2 peak phase, **b** RCs 1–2 transition phase, **c** RCs 3–4 peak

phase, **d** RCs 3–4 transition phase. Contour interval is 0.04 K . Stippling indicates those grid boxes where a t-test on the mean of the events in the composite (3 for RCs 1–2, 4 for RCs 3–4) exceeds the 99% significance level

pled ocean-atmosphere GCM. It is associated with the only interdecadal peak in the spectrum of North Pacific SST that differs from an appropriate red-noise spectrum at the 95% confidence level. The oscillation is irregular, but the underlying near-periodicity has a maximum amplitude of about 0.2 K in SST and 5 m in 500 hPa geopotential; it is most active around years 100 and 300. The oscillation is characterized by a predominantly standing oscillation in the atmosphere peaking west of the dateline, with positive heights at 500 hPa overlying positive SST anomalies; there is a small westward tilt with height. Sub-surface anomalies, by contrast, propagate distinctly northward and have a spatial structure and evolution that is suggestive of Rossby wave adjustment, strongly modified by the atmosphere.

The model's 18-y oscillation has a similar period to that already identified in a shorter integration of the same GCM by von Storch (1994) using a POP analysis of sea level. That mode, however, appeared not to have its origin in mid-latitudes, and its connection with that found here is unclear. The oscillation period and structure in this study also bear similarity with those recently found by Latif and Barnett (1994) in a 70-y integration of the higher-resolution (T42) ECHO model. The latter mode has larger amplitude, which may be related to better resolution of the atmospheric baroclinic eddies. Latif and Barnett (1994) also found a downstream signature over North America, while no such teleconnections could be found in the present model.

To gauge the relevance of the model's oscillation to the real world, M-SSA was applied to the GISST observational SST dataset, which spans the period 1871–1992. Two interannual oscillatory components, with periods of about 6 and roughly 30 y, were detected over the North Pacific, although only the 6-y component is statistically significant with respect to a red-noise null hypothesis. In terms of spatial pattern, both components consist primarily of a stationary monopole anomaly that resembles the one found in the model; the principal difference being that both GISST anomalies extend much further eastward, while the model's SST anomaly is confined to the western Pacific.

No statistically significant counterpart to the model's 18-y periodicity was found in the GISST dataset. Nevertheless, Fig. 13 indicates that the GISST has broad power in the 20–50 y band, and the more refined testing strategy of Allen and Smith (1996) may be capable of isolating a comparable period. An improved version of the GISST data set is currently being developed (M. K. Davey, personal communication 1995), and this too may enable decadal fluctuations to be detected with statistical confidence. On the other hand it is interesting to note that the spectrum of the GCM's raw SST over the western Pacific (Fig. 5b) does have peaks at around 30 and 9 y. An M-SSA of the GCM's SST field for a broader frequency interval than the one used to reconstruct the 18-y mode does isolate a leading RC-pair with a period of about 37 y, together with a weaker component at around 9 y. Although neither

is statistically significant, the SST anomaly pattern associated with the 37-y component is more zonally extensive than that of the 18-y mode, more in agreement with the GISST pattern.

Does the coupled GCM's 18-y oscillation have its origin in the model atmosphere or ocean, or is ocean-atmosphere interaction fundamental? While a definitive answer must await tests with simplified models, the following factors point to the importance of ocean-atmosphere interaction.

1. Atmospheric anomalies peak when the northward-propagating thermocline anomaly aligns with the model's broad Kuroshio extension region which lies between 30–40°N. This suggests that the model atmosphere is reacting to changes in the ocean, and this is partially substantiated by the indication that sub-surface thermal advection to the southwest of the region of the maximum SST anomaly, leads the latter and the atmospheric anomaly by about one-quarter period.
2. The largest sub-surface anomalies lag the peak of the atmospheric anomaly by about 4 y or about one-quarter period. This suggests that the delay associated with oceanic adjustment and advection influence the period of the oscillation; the latter is consistent with the advective and spin-up time scales of the subtropical gyre, as discussed by Latif and Barnett (1994).
3. Over a large region to the southeast of the warm SST anomaly maximum, there is a compensation between the anomalous surface heat flux out of the ocean, and anomalous warm advection in the ocean surface layer. Palmer and Sun (1985) proposed that this configuration could allow persistence, and this appears to be the case in the coupled GCM. The classical linear response of the atmosphere to a low-level heating in mid-latitudes is a baroclinic one, with the surface anticyclone situated due west of the heat source (e.g., Hoskins and Karoly 1981). Descent over the heat source balances planetary vorticity advection associated with southward flow at low levels, while the vertical structure can either be baroclinic or equivalent barotropic, depending on the strength of the zonal flow aloft. In the coupled GCM, the surface anticyclone is centered to the *northwest* of the low-level atmospheric heat source. This displacement of the heating anomaly to the south of the anticyclone indicates the importance of oceanic thermal advection by Ekman currents as discussed by Miller (1992). The combination of this southward displacement of the SST and heating anomalies, together with the westward displacement of the SST anomaly strongly suggests the role of air-sea interaction. Exactly how this comes about requires further work, but the effects of baroclinic eddies are likely to be important.

Acknowledgements. The author is indebted to the Max Planck Institute in Hamburg for making available the coupled GCM integration, and to J. S. and H. von Storch for their kind assistance. The use of the UK Meteorological Office's GISST SST dataset (from D. Parker and the Hadley Centre Climate Data Monitoring Group) is gratefully acknowledged, and I thank M. Davey for providing me with it. It is a pleasure to thank M. Ghil, M. Kimoto, M. Latif, and J. D. Neelin for helpful discussions, and M. Allen

for sharing his statistical expertise with me. P. Lenzen's help with the model output was invaluable. This work was supported by the University of California's INCOR program, and by NOAA grant NA46GP0244.

Appendix A: M-SSA and the Monte Carlo test

Signal detection

The reader is referred to Allen and Robertson (1995 submitted) and Robertson et al. (1995) for a full explanation of this test, which uses a simple Monte Carlo approach. First, we generate a large ensemble of red-noise surrogate data segments, that have the same length, number of channels, and same lag-1 temporal and spatial auto-correlations as our sample time series. Second, we project both our sample and each of the noise surrogates onto a common basis and compare the power in the individual basis vectors. We thereby test whether there is significantly more power in the projections of our sample time series onto a particular basis vector (i.e., along a particular line in phase space) than we would expect to find had the GCM time series been generated by the hypothetical noise process. If so, and if that vector is dominated by a single frequency, this may indicate a genuine oscillation.

The choice of basis is motivated by M-SSA. Central to SSA is the concept of windowing of time series to enhance the signal-to-noise (S/N) ratio by limiting the spectral resolution and bandwidth (Broomhead and King 1986; Vautard and Ghil 1989). First the time series is windowed to form an "augmented data matrix" by sliding a (univariate) window of prescribed length N_w down the L channels of a uniformly sampled time series of length N consecutively. This yields a series of N_w -variate vectors that are the $(N - N_w + 1)L$ "views" of the time series, and these vectors form the columns of the augmented data matrix \mathbf{X} (Broomhead and King 1986). This matrix is rectangular with N_w rows and $(N - N_w + 1)L$ columns, and a singular value decomposition (SVD) of \mathbf{X} yields two orthogonal bases, the temporal principal components (T-PCs) and spatio-temporal EOFs (ST-EOFs):

$$\mathbf{X} = \mathbf{P}\mathbf{\Lambda}^{1/2}\mathbf{Q}^T \quad (\text{A.1})$$

The T-PCs are the left-singular vectors of \mathbf{X} , given by the columns of \mathbf{P} ; the columns of \mathbf{Q} are the right-singular vectors, or ST-EOFs; and $\mathbf{\Lambda}$ is diagonal with the associated variances as its entries. For the length of time series considered here and most choices of N_w , $(N - N_w + 1)L > N_w$ so only the T-PCs form a *complete* basis. This is crucial because it determines the rank and physical meaning of the basis in which to perform the test, namely the $N_w \times N_w$ basis of T-PCs. The projection of the windowed time series onto the k th basis vector \mathbf{p}_k is then given by

$$\lambda_k = \mathbf{p}_k^T \mathbf{X} \mathbf{X}^T \mathbf{p}_k \quad (\text{A.2})$$

For unbiased signal detection, it turns out that the most appropriate basis onto which to project is not the basis \mathbf{P} constructed from the GCM data, but rather

that appropriate to the AR(1) null-hypothesis. This amounts to assuming that the GCM time series is noise, until shown otherwise (Allen and Smith 1996). Since we are concerned with a basis of *univariate* T-PCs, it is straightforward to construct the appropriate basis for an AR(1) process. For a univariate AR(1) process with lag-1 autocorrelation γ , and variance c_0 , this basis consists of the eigenmodes of the process lag-covariance matrix $c_0 \mathbf{W}$ where $W_{i,j} = \gamma^{|i-j|}$. The basis vectors are sinusoids with frequencies $f_k \approx 1/2N_w, 1/N_w, 3/2N_w, \dots, 1/2$, where N_w is the length of the basis vectors and the rank of the basis (Allen 1992). Figure 2 shows how these sample frequencies are in practice very evenly spaced in frequency with a spacing equal to the spectral resolution.

Selecting N_w , which corresponds to the window length, involves the usual trade-off between the degree of S/N enhancement, which increases with rank of the basis, i.e., the length of the window, and statistical robustness that decreases as the window is lengthened (because the projection is an average over fewer, longer, windowed time-series segments). In addition, a phase-modulated oscillation will only yield a large projection if the window is shorter than the average lifetime of its spells (Vautard et al. 1992).

To make the test as stringent as possible, not only do we have to account for the fact that the model time series is red in both space and time, but also that the largest spatial scales are associated with the largest decorrelation times. This is accomplished most easily by working in the space of the spatial PCs (S-PCs) of the GCM time series by means of a spatial EOF (S-EOF) decomposition: we take the leading 10 S-PCs as our channels instead of the spatial grid points themselves (Ghil and Mo 1991). Thus each surrogate data segment is constructed to consist of 10 channels, each being a (centered) univariate AR(1) process whose variance and lag-1 autocorrelation are chosen to match those of the respective S-PC of the data. In this way decorrelation times of the surrogates are effectively spatial-scale-dependent because the highest-ranked S-PCs have the largest decorrelation times and correspond to S-EOFs with the largest spatial scales.

The test is applied to 4-y means of SST over the North Pacific, decomposed in terms of the leading 10 S-PCs, each of length $N = 125$ (4-y means). This retains 69.9% of the total SST variance; the results are insensitive to retaining 20 S-PCs. The AR(1) process-basis is defined using a channel-averaged variance c_0 , and a channel-variance weighted value of γ ; the 10 S-PCs of 4-y mean SST yield $\gamma = 0.40$. For high spectral resolution, a window length of $N_w = 115$, is chosen; at lower resolutions, the peaks identified in Figs. 2 and 13 become less well resolved.

Signal reconstruction

In contrast to the task of unbiased signal detection, the most efficient basis for *reconstructing* an oscillation is the optimal basis of the data series itself, \mathbf{P} in Eq. (A.

1), which is obtained by an SVD of \mathbf{X} . Expansion of the time series with respect to this $N_W \times N_W$ basis defines M-SSA, and provides the means of reconstructing weak oscillatory signals. For the signal detection algorithm we were free to choose a very large value of N_W to maximize the spectral resolution and S/N ratio. However, the optimal SVD basis itself depends on N_W . To reconstruct the spells of a phase and amplitude modulated oscillation, the window length should lie in between the period of the oscillation, and the duration of its spells, exactly as in the single channel case (Vautard et al. 1992). Choosing to reconstruct the GCM's oscillation using annual means, $N_W = 50$ proved to be a good compromise between adequate spectral resolution (larger N_W) and retaining aspects of phase and amplitude modulation (smaller N_W). The main features of the reconstruction are insensitive to halving or doubling this value. However, the reconstruction became increasingly irregular as the window length is decreased toward the period of the oscillation, providing a measure of the irregular character of the GCM's oscillation. By using a larger value of N_W , we increasingly average out these irregularities. When the basis vectors, the T-PCs, become short, the T-EOFs lengthen accordingly, and it is the latter that represent the data-adaptive modulation of an oscillatory signal over time.

Appendix B: pre-filtering

A simple 5-y running mean is used to exclude the highest frequencies. To remove the lowest frequencies, Vautard et al. (1992) have shown how single-channel SSA can be used to identify "trend" components, or periods greater than a specified window-length, in a time series, in terms of the leading pair of eigenelements. Their approach, however, is only effective if there is a clear separation between the eigenelements associated with a sizable "trend", and those associated with the signal of interest. If, on the other hand, the spectrum has a strong red component, the data-adaptive nature of SSA can cause degeneracy between the leading "trend" eigenelements, and those of an oscillatory signal of interest (Allen 1992).

We take a related approach to detrend the time series, removing components with periods greater than 25 y. At each grid point, two filtered time series are subtracted using running-mean filters of length 25 y whose weights are (1) a constant, and (2) a constant gradient (M. R. Allen, personal communication). The point of using these two particular filters, is that they correspond to Vautard et al.'s (1992) SSA detrending algorithm, but with the shape of the two "trend" eigenvectors specified to be linear, with zero and non-zero gradient respectively. By fixing their shape, the "trend" eigenelements cannot become degenerate with those of the "signal". As an aside, this detrending procedure can also be performed in a multichannel context; in this case the temporal shape of the space-time EOFs (ST-EOFs) is fixed to be linear as in the single-

channel case, whilst the spatial form is determined data-adaptively via an EOF analysis. The multichannel case is equivalent to the single channel one when all these EOFs are included in the "trend" ST-EOFs.

References

- Allen MR (1992) Interactions between the atmosphere and oceans on time scales of weeks to years. PhD Thesis, University of Oxford, UK
- Allen MR, Smith LA (1994) Investigating the origins and significance of low-frequency modes of climate variability. *Geophys Res Lett* 21:883–886
- Allen MR, LA Smith (1996) Monte Carlo SSA: detecting irregular oscillations in the presence of colored noise. *J Clim* (accepted)
- Bjerknes J (1964) Atlantic air-sea interactions. *Adv Geophys* 1–82
- Broomhead DS, King GP (1986) Extracting qualitative dynamics from experimental data. *Physica D* 20:217–236
- Cubasch U, Hasselmann K, Hoock H, Maier-Reimer E, Mikolajewicz U, Santer BS, Sausen R (1992) Time-dependent greenhouse warming computations with a coupled ocean-atmosphere model. *Clim Dyn* 8:55–69
- Dettinger MD, Strong CM, Weibel W, Ghil M, Yiou P (1995) Software for singular spectrum analysis of noisy time series. *Eos Trans AGU* 76(2) pp 12, 14, 21
- Dickson RR, Namias J (1976) North American influences on the circulation and climate of the North American sector. *Mon Weather Rev* 110:1851–1862
- Douglas AV, Cayan DR, Namias J (1982) Large-scale changes in North Pacific and North American weather patterns in recent decades. *Mon Weather Rev* 112:1255–1265
- Frankignoul C (1985) Sea surface temperature anomalies planetary waves and air-sea feedback in middle latitudes. *Rev Geophys* 8:233–246
- Ghil M, Mo KC (1991) Intraseasonal oscillations in the global atmosphere Part I: northern hemisphere and tropics. *J Atmos Sci* 48:780–789
- Graham NE (1994) Decadal-scale climate variability in the tropical North Pacific during the 1970s and 1980s; observations and model results. *Clim Dyn* 10:135–162
- Hoskins BJ, Karoly DJ (1981) The steady linear response of a spherical atmosphere to thermal and orographic forcing. *J Atmos Sci* 38:1179–1196
- Latif M, Barnett TP (1994) Causes of decadal climate variability over the North Pacific/North American sector. *Science* 266:634–637
- Maier-Reimer E, Mikolajewicz U, Hasselmann K (1993) Mean circulation of the Hamburg LSG OGCM and its sensitivity to the thermohaline surface forcing. *J Phys Oceanogr* 23:731–757
- Miller AJ (1992) Large-scale ocean-atmosphere interactions in a simplified coupled model of the midlatitude wintertime circulation. *J Atmos Sci* 49:273–286
- Namias J (1959) Recent seasonal interactions between North Pacific waters and the overlying atmospheric circulation. *J Geophys Res* 64:631–646
- Palmer TN, Sun Z (1985) A modelling and observational study of the relationship between sea surface temperature in the north-west Atlantic and the atmospheric general circulation. *Q J R Meteorol Soc* 111:947–975
- Parker DE, Folland CK, Bevan A, Ward MN, Jackson M, Maskell K (1994) Marine surface data for analysis of climatic fluctuations on interannual to century timescales. In: Martinson DG, Bryan K, Ghil M, Hall MM, Karl TR, Sarachik ES, Sorostian S, Talley LF (eds) *Natural climate variability on decade to century time scales*. National Academy Press, Washington, USA

- Plaut G, Vautard R (1994) Spells of low-frequency oscillations and weather regimes in the Northern Hemisphere. *J Atmos Sci* 51:210–236
- Robertson AW, Allen MR, Ghil M, Smith LA (1995) Tests for distinguishing multivariate oscillatory behavior from noise. Proc 19th Climate Diagnostics Workshop, College Park, Maryland. Climate Analysis Center, NOAA
- Sausen R, Barthel K, Hasselmann K (1988) Coupled ocean-atmosphere models with flux corrections. *Clim Dyn* 2:154–163
- Sezginer Y, Ghil M (1995) Interannual and interdecadal oscillations patterns in sea level. *Clim Dyn* 11:255–278
- Tanimoto Y, Iwasaka N, Hanawa K, Toba Y (1993) Characteristic variations of sea surface temperature with multiple time scales in the North Pacific. *J Clim* 6:1153–1160
- Thomson DJ (1990) Time series analysis of Holocene climate data. *Philos Trans R Soc London an A* 330:601–616
- Trenberth KE (1990) Recent observed interdecadal climate changes in the Northern Hemisphere. *Bull Am Meteorol Soc* 71:988–993
- Trenberth KE, Hurrell JW (1994) Decadal atmosphere-ocean variations in the Pacific. *Clim Dyn* 9:303–319
- Vautard R, Ghil M (1989) Singular spectrum analysis in nonlinear dynamics with applications to paleoclimatic time series. *Physica D* 35:395–424
- Vautard R, Yiou P, Ghil M (1992) Singular-spectrum analysis: a toolkit for short noisy chaotic signals. *Physica D* 58:95–126
- von Storch JS (1994) Interdecadal variability in a global coupled model. *Tellus* 46A:419–432
- Wallace JM, Smith C, Jiang Q (1990) Spatial patterns of atmosphere-ocean in the northern winter. *J Clim* 3:990–998
- White WB, Barnett TP (1972) A servomechanism in the ocean/atmosphere system of the mid-latitude North Pacific. *J Phys Oceanogr* 2:372–381
- Xu JS (1993) The joint modes of the coupled atmosphere-ocean system observed from 1967 to 1986. *J Clim* 6:816–838